Journal of the Mechanical Behavior of Biomedical Materials 169 (2025) 107042

Contents lists available at ScienceDirect

Journal of the Mechanical Behavior of Biomedical Materials

journal homepage: www.elsevier.com/locate/jmbbm

Research paper

A microstructural material model for adipose tissue under blunt impact considering different types of loading

Felicitas Lanzl [a,b,*], Steffen Peldschus [a], Gerhard A. Holzapfel [c,d], Fabian Duddeck [b] and Gerhard Sommer [c]

[a] Biomechanics and Accident Analysis, Institute of Legal Medicine, Ludwig-Maximilians-Universität München, Germany
[b] School of Engineering and Design, Technische Universität München, Germany
[c] Institute of Biomechanics, Graz University of Technology, Austria
[d] Department of Structural Engineering, Norwegian University of Science and Technology, Trondheim, Norway

ARTICLE INFO

Keywords:
Adipose tissue
Microstructural material model
Blunt impact
Combined loading

ABSTRACT

Modeling of subcutaneous adipose tissue (SAT) plays an important role in forensic biomechanics as blunt force trauma represents one of the most common types of injury. To better understand the involved injury mechanisms, a material model is needed that can (i) represent realistic behavior for combined loading scenarios and (ii) consider the microstructure of the SAT. Therefore, a SAT model was developed that consists of two parts for the strain–energy function – a neo-Hookean part representing the adipocytes and a part representing the surrounding reinforced basement membrane, which is modeled via three circular fiber families oriented in the three main planes, resulting in isotropic model behavior. To verify the performance of the model, the analytical and numerical model solution were compared with experimental data under biaxial tension at different stretch ratios (1 : 1, 1 : 0.5, 0.5 : 1) and under simple shear using an objective evaluation method. The material parameters were evaluated by fitting to the data under equibiaxial tension. For the numerical analysis, the model was implemented as a user-defined material in LS-DYNA to simulate the respective experimental setups. The analytical fitting of the model was robust. Using the resulting material parameters, both the analytical and numerical simulation results were able to represent the experimental data under biaxial tension as well as under simple shear quite well. Since the fitting was only performed with data under equibiaxial tension, these findings suggest that the model assumptions are reasonable. Therefore, the model could help to further investigate the injury mechanisms in blunt impacts.

1. Introduction

Subcutaneous adipose tissue (SAT) is the loose connective tissue just beneath the dermis of the skin (Alkhouli et al., 2013). As one of the outermost layers of the human body, SAT alters the stresses and strains transmitted to underlying bones or organs during blunt impacts, and thus also influences the risk of injury to these tissues (Comley and Fleck, 2012; Dempsey and Blau, 2020). Different studies suggest that skin and SAT in combination can reduce the impact energy during blunt impacts to the human body by 30 % up to 69 % (Gurdjian, 1972; Nikolić et al., 1975; Trotta et al., 2018). Therefore, a deeper understanding of the mechanical behavior of SAT under blunt impact is relevant for various fields of biomechanics, especially in forensics, where blunt force trauma is one of the most common types of injury (Quatrehomme and Alunni, 2019; Dempsey and Blau, 2020). Nevertheless, little is known about the injury mechanisms in detail and objective methods to evaluate the impact forces occurring are lacking (Sharkey et al., 2012; Dempsey and Blau, 2020). A promising tool to analyze the impact of SAT on the injury risk of underlying structures during blunt impact is the finite element (FE) method. Unlike experimental methods, ethical issues can be avoided and, more importantly, mechanical behavior can be assessed at the tissue level (Cronin, 2011; Dempsey and Blau, 2020). However, the potential to use FE models for such analyses strongly depends on the quality and validity of the material modeling of the involved tissues (Cronin, 2011). Adequate modeling for biological soft tissues remains challenging as they exhibit complex material properties that are closely linked to the tissue microstructure.

One of the most important structural elements of SAT are adipocytes, which are embedded in a three-dimensional extracellular matrix (Comley and Fleck, 2010a; Alkhouli et al., 2013). Adipocytes are lipid-filled cells with a nearly spherical shape that exhibit a diameter

* Corresponding author at: Biomechanics and Accident Analysis, Institute of Legal Medicine, Ludwig-Maximilians-Universität München, Germany.
E-mail address: felicitas.lanzl@med.uni-muenchen.de (F. Lanzl).

https://doi.org/10.1016/j.jmbbm.2025.107042
Received 12 December 2024; Received in revised form 29 April 2025; Accepted 1 May 2025
Available online 19 May 2025

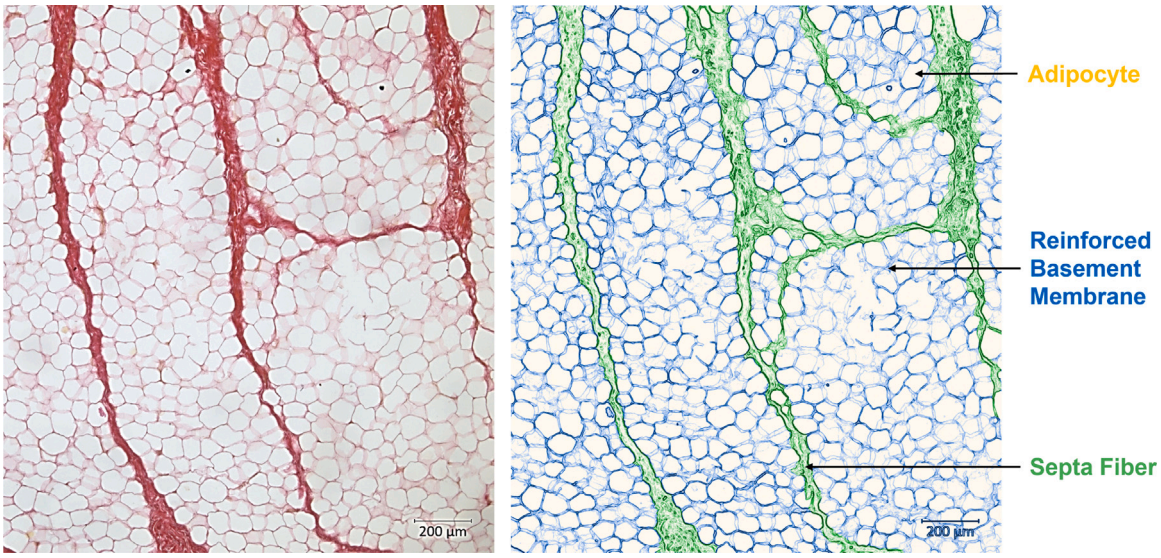

Fig. 1. Original (left) and processed (right) histological images of subcutaneous adipose tissue of the human scalp (Elastica van Gieson (EvG) stain). Since EvG staining highlights all collagenous structures in red, the image was digitally processed to enhance the visual differentiation of the main microstructural components. Adipocytes are depicted in light yellow, the reinforced basement membrane surrounding each adipocyte is shown in blue, and the long septa fibers penetrating the tissue are shown in green.

between 50 and 80 µm (Comley and Fleck, 2010a; Sommer et al., 2013). Their interior is almost completely filled by a vacuole of triglyceride lipid (Sheldon, 2011). Their exterior is surrounded by a basement membrane consisting of a thin sheet of non-fibrillar collagen, which in turn is encapsulated by a second, thicker layer of fibrillar collagen that forms a dense fiber network around the adipocytes (Comley and Fleck, 2010b; Chun, 2012; Alkhouli et al., 2013). Thus, each adipocyte is enclosed by both the basement membrane and the fibrillar network, creating a foam-like extracellular structure (Comley and Fleck, 2010a), which is referred to in the present study as reinforced basement membrane (RBM) according to the work of Comley and Fleck (Comley and Fleck, 2010a, 2012). The second major structure of the extracellular matrix of SAT are long collagen fibers that permeate the tissue microstructure (Comley and Fleck, 2010b; Chun, 2012). They are also called septa fibers and have a similar composition to the collagen fibers in the dermis of the skin (Comley and Fleck, 2010a; Alkhouli et al., 2013). Thus, the microstructure of SAT essentially consists of three main components considered relevant during mechanical loading: (i) the adipocytes, (ii) the RBM and (iii) the septa fibers. The microstructural organization of collagenous structures in the tissue is depicted in Fig. 1.

This complex microstructure influences the macroscopic material behavior of the SAT. The tissue behaves nonlinear, which was observed under uniaxial compression (Comley and Fleck, 2012; Calvo-Gallego et al., 2018; Sun et al., 2021a,b), uniaxial tension (Comley and Fleck, 2012; Alkhouli et al., 2013; Sree et al., 2023), biaxial tension (Sommer et al., 2013) as well as simple shear (Sommer et al., 2013; Sun et al., 2021a,b). In addition, the tissue exhibits a strain rate dependent behavior, which has been demonstrated for uniaxial compression (Comley and Fleck, 2012; Calvo-Gallego et al., 2018; Sun et al., 2021a), biaxial tension (Sommer et al., 2013) and simple shear (Sun et al., 2021a). Besides, its material response in simple shear is relatively soft compared to that in uniaxial compression or biaxial tension (Sommer et al., 2013; Sun et al., 2021a,b). Various hyperelastic models have been used to depict the material behavior of SAT, e.g., the neo-Hookean model (Payne et al., 2015; Naseri et al., 2018), the Mooney–Rivlin model (Payne et al., 2015; Sun et al., 2019), the first-order Ogden model (Comley and Fleck, 2012; Calvo-Gallego et al., 2018; Trotta and Ní Annaidh, 2019), the Yeoh model (O'Hagan and Samani, 2009) or the polynomial model (Calvo-Gallego et al., 2018).

However, to the authors' knowledge, only Sommer et al. (2013) and Sun et al. (2021a,b) have evaluated model performance for more than one loading type. Sommer et al. (2013) fitted an anisotropic, hyperelastic model for fiber reinforced soft tissues to the experimental response of SAT under biaxial tension and simple shear, while Sun et al. (2021b) fitted a first-order Ogden model to data under uniaxial compression and simple shear. Both found that the fits for each loading type resulted in different material parameter sets. Therefore, in Sommer et al. (2013) additionally a combined fit to the data under biaxial tension as well as simple shear was performed. However, this resulted in a less accurate fit to the experimental data compared to the fitting results for only one loading type, suggesting that material modeling of SAT proves difficult for scenarios involving a combination of different loading types. However, blunt impact actually represents such a scenario, as the vector of the impact force is generally not exactly normal to the body surface, resulting in a combined loading. To further address this issue, Sun et al. (2021a) performed a combined fit to data under uniaxial compression and simple shear in a subsequent study and found that a third-order Ogden model could capture the material behavior for both loading conditions quite well. However, the Ogden model is purely phenomenological and does not take into account the microstructure of the SAT, which is considered essential for a deeper understanding of injury mechanisms in blunt impacts. Therefore, the aim of this study is to develop a material model for SAT that is capable to (i) reproduce realistic material behavior under different loading types and (ii) to account for the specific microstructure of the SAT.

2. Material model

2.1. Theory

Model development is based on the assumption that the macroscopic deformation of SAT is strongly linked to the behavior of its microstructural components. It is hypothesized that in the initial phase of an impact, the lipid inside of the adipocytes is compressed, causing the adipocyte cell walls and thus also the surrounding RBM to stretch biaxially in the plane perpendicular to the loading direction. This leads to a tensile load and thus to an activation of the collagen fibrils within the RBM. As the impact progresses, the adipocytes deform more and more into an elliptical shape until the main load is borne by the collagenous structures of the RBM (Lanzl et al., 2022). The load is additionally supported by the septa fibers, which are assumed to be activated and reoriented during the impact, similar to the behavior

of the collagen fiber network in the dermis of the skin (Daly, 1982; Holzapfel, 2001; Kieser, 2012). The slightly anisotropic behavior of the SAT is probably also determined by these septa fibers (Sommer et al., 2013). However, for the development of a first version of the model, the contribution of the septa fibers is neglected, since the RBM probably has a greater influence on the bulk mechanical behavior due to a higher volume fraction compared to the septa fibers in the SAT (Comley and Fleck, 2010a).

The presented model, referred to as the circular fiber model (CFM) in this work, is developed in the framework of three dimensional, nonlinear continuum mechanics and the SAT is treated as a homogeneous, incompressible, hyperelastic material. Therefore, the material behavior can be described by a strain–energy function (SEF) (Holzapfel, 2000). It is assumed that the SEF for the model, say Ψ_{CFM}, can be additively decomposed into two parts corresponding to the two microstructural elements considered for model development — one part for the lipid-filled adipocytes Ψ_{Lipid} and one part for the RBM Ψ_{RBM}, i.e.

$$\Psi_{\mathrm{CFM}} = \Psi_{\mathrm{Lipid}} + \Psi_{\mathrm{RBM}}. \tag{1}$$

The SEF Ψ_{Lipid} representing the behavior of the lipid-filled adipocytes is modeled as a neo-Hookean material (Treloar, 1943, 1944; Rivlin and Taylor, 1948), i.e.

$$\Psi_{\mathrm{Lipid}} = \frac{c}{2}(\lambda_1^2 + \lambda_2^2 + \lambda_3^2 - 3), \tag{2}$$

where λ_1, λ_2, λ_3 depict the stretches in the three principal directions and c the shear modulus in the undeformed state, see, e.g., Holzapfel (2000).

The SEF Ψ_{RBM} representing the RBM is based on the assumption that the membrane consists of several collagen fibrils surrounding each adipocyte in random orientation. These orientations are supposed to be evenly distributed across the membrane and hence the fiber network can be simplified into three circular fiber families surrounding each adipocyte and oriented in the three principal planes of the coordinate system as illustrated in Fig. 2. Furthermore, the contribution of each fiber family is expected to be equal and can be summed up to account for the bulk mechanical behavior of the RBM as the mechanical properties of the different collagen fibers are assumed to be similar. Therefore, the isotropic SEF for the RBM is

$$\Psi_{\mathrm{RBM}} = \sum_{i=1}^{3} \frac{k_1}{2k_2}\left\{\exp[k_2(\lambda_{\mathrm{CF},i} - 1)^2] - 1\right\}, \tag{3}$$

where k_1 and k_2 are material parameters with and without stress dimensions, respectively. The mathematical representation for each fiber family is based on the fiber term of the model by Holzapfel et al. (2000).

For the presented material model, however, the expression for the fiber stretch has to be modified, since it describes the behavior of a circular and not a linear fiber structure. For a circular fiber (CF), the fiber stretch $\lambda_{\mathrm{CF},i}$ does not only depend on the stretch in one principal direction, but on a combination of the stretches in two principal directions. These two directions represent the axes of the circular fiber, which deforms into an ellipse under load. Thus, the fiber stretches $\lambda_{\mathrm{CF},i}$, $i = 1, 2, 3$, can be expressed by the mathematical approximation for the perimeter of an ellipse $p_{\mathrm{ellipse}} = 2\pi(0.5a^2 + 0.5b^2)^{1/2}$, where a and b are the semi-axes of the ellipse (compare with Fig. 2).

Similar to the model of Holzapfel et al. (2000), each fiber family is assumed to contribute to the mechanical behavior of the RBM only when the fiber is under tension. Taking these assumptions into account, the fiber stretch $\lambda_{\mathrm{CF},i}$, $i = 1, 2, 3$, can be expressed by the following conditions

$$\lambda_{\mathrm{CF},1} = \begin{cases} (\lambda_1^2 + \lambda_2^2)/2, & \text{if } \lambda_1^2 + \lambda_2^2 \geq 2 \\ 1, & \text{if } \lambda_1^2 + \lambda_2^2 < 2, \end{cases} \tag{4}$$

$$\lambda_{\mathrm{CF},2} = \begin{cases} (\lambda_2^2 + \lambda_3^2)/2, & \text{if } \lambda_2^2 + \lambda_3^2 \geq 2 \\ 1, & \text{if } \lambda_2^2 + \lambda_3^2 < 2, \end{cases} \tag{5}$$

$$\lambda_{\mathrm{CF},3} = \begin{cases} (\lambda_1^2 + \lambda_3^2)/2, & \text{if } \lambda_1^2 + \lambda_3^2 \geq 2 \\ 1, & \text{if } \lambda_1^2 + \lambda_3^2 < 2, \end{cases} \tag{6}$$

where λ_1, λ_2 and λ_3 represent here the global stretches in the three principal directions. The following restrictions hold for the material parameters: $c \geq 0$, $k_1 \geq 0$, $k_2 \geq 0$.

2.2. Finite element implementation

To implement the model in a FE environment, a nearly incompressible material behavior is assumed and a deviatoric and volumetric decomposition is performed. For the volumetric term of the strain–energy function, e.g., the following formula is used (Gültekin et al., 2019)

$$\Psi_{\mathrm{CFM}} = \frac{\bar{c}}{2}(\bar{\lambda}_1^2 + \bar{\lambda}_2^2 + \bar{\lambda}_3^2 - 3) + \sum_{i=1}^{3} \frac{\bar{k}_1}{2\bar{k}_2}\left\{\exp[\bar{k}_2(\bar{\lambda}_{\mathrm{CF},i} - 1)^2] - 1\right\} + \kappa(J - \ln J - 1), \tag{7}$$

where $\bar{c}$, $\bar{k}_1$, $\bar{k}_2$ are material parameters, $\bar{\lambda}_i = J^{-1/3}\lambda_i$, $i = 1, 2, 3$, represent the modified principal stretches, J represents the Jacobian determinant and κ is the bulk modulus of the adipose tissue (Holzapfel, 2000). The model was implemented as a user-defined material model in the explicit FE solver LS-DYNA (version R9.1, Livermore Software Technology, USA) via a FORTRAN 77 subroutine (Intel Fortran Compiler, version 18.0, Intel Corporation, USA). In this subroutine, the Cauchy stress tensor $\boldsymbol{\sigma}$ is calculated from the deformation gradient $\mathbf{F}$ provided as input by the solver.

3. Methods

3.1. Analytical solution and material parameter identification

In a first step, the analytical solution for the incompressible CFM, i.e. Eq. (1), was investigated under both biaxial tension and simple shear. To derive the analytical solution under biaxial tension, a thin SAT sheet is considered that is equibiaxially stretched along the first and the second principal directions and assumed to be in a state of plane stress during deformation. By calculating the hydrostatic pressure as $p = \lambda_3(\partial\Psi/\partial\lambda_3)$ and incorporating the incompressibility condition $\lambda_1\lambda_2\lambda_3 = 1$ (Holzapfel, 2000), the Cauchy stress components σ_1 and σ_2 under equibiaxial tension for the CFM are determined as

$$\begin{aligned} \sigma_1 &= c(\lambda^2 - \lambda^{-4}) \\ &+ k_1\lambda^2\left\{\exp[k_2(\lambda_{\mathrm{CF},1} - 1)^2](\lambda_{\mathrm{CF},1} - 1) + \exp[k_2(\lambda_{\mathrm{CF},3} - 1)^2](\lambda_{\mathrm{CF},3} - 1)\right\} \\ &- k_1\lambda^{-4}\left\{\exp[k_2(\lambda_{\mathrm{CF},2} - 1)^2](\lambda_{\mathrm{CF},2} - 1) + \exp[k_2(\lambda_{\mathrm{CF},3} - 1)^2](\lambda_{\mathrm{CF},3} - 1)\right\}, \end{aligned} \tag{8}$$

$$\begin{aligned} \sigma_2 &= c(\lambda^2 - \lambda^{-4}) \\ &+ k_1\lambda^2\left\{\exp[k_2(\lambda_{\mathrm{CF},1} - 1)^2](\lambda_{\mathrm{CF},1} - 1) + \exp[k_2(\lambda_{\mathrm{CF},2} - 1)^2](\lambda_{\mathrm{CF},2} - 1)\right\} \\ &- k_1\lambda^{-4}\left\{\exp[k_2(\lambda_{\mathrm{CF},2} - 1)^2](\lambda_{\mathrm{CF},2} - 1) + \exp[k_2(\lambda_{\mathrm{CF},3} - 1)^2](\lambda_{\mathrm{CF},3} - 1)\right\}. \end{aligned} \tag{9}$$

To derive the analytical solution under simple shear, a thin SAT sheet is assumed to experience a deformation given by the deformation gradient $\mathbf{F} = \mathbf{I} + \gamma\mathbf{e}_1 \otimes \mathbf{e}_2$, where γ is the amount of shear, $\mathbf{I}$ denotes the second-order unit tensor, while $\mathbf{e}_1$ and $\mathbf{e}_2$ are the related base vectors. By calculating the in-plane stretches by solving the characteristic equation $\det(\mathbf{b} - \lambda^2\mathbf{I})$ and evaluating the corresponding eigenvectors of the left Cauchy–Green tensor $\mathbf{b} = \mathbf{F}\mathbf{F}^{\mathrm{T}}$ (Holzapfel, 2000; Horgan and

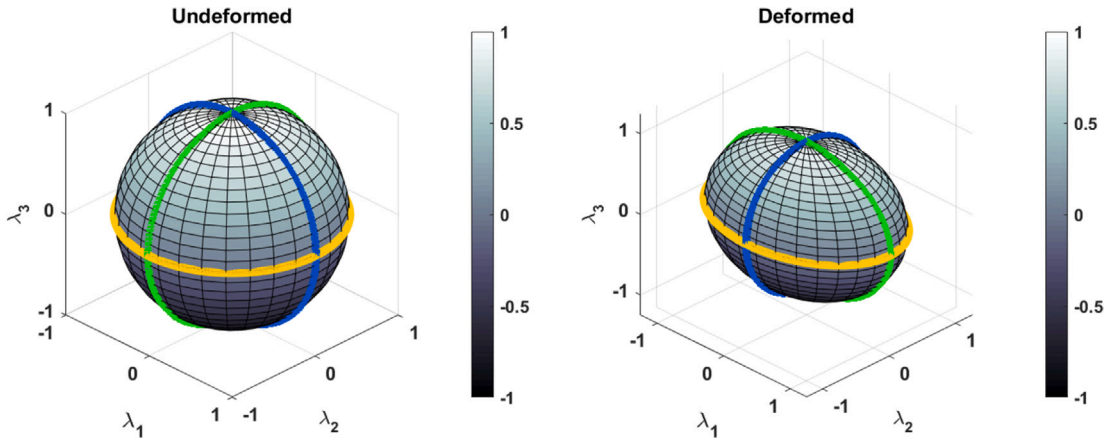

Fig. 2. Schematic representation of the three circular fibers (blue, yellow and green) aligned in the principal planes. The total fiber stretch depends on a combination of the stretches in two principal directions corresponding to the axes of the circular fiber.

Murphy, 2010), the Cauchy stress component σ_{12} for the CFM under simple shear can be expressed as

$$\begin{aligned}\sigma_{12} = &\frac{\lambda_1^3}{\lambda_1^2+1}\left\{c + k_1\left[\exp[k_2(\lambda_{CF,1}-1)^2](\lambda_{CF,1}-1)\right.\right.\\ &\left.\left.+\exp[k_2(\lambda_{CF,3}-1)^2](\lambda_{CF,3}-1)\right]\right\}\\ &-\frac{\lambda_2^3}{\lambda_2^2+1}\left\{c + k_1\left[\exp[k_2(\lambda_{CF,1}-1)^2](\lambda_{CF,1}-1)\right.\right.\\ &\left.\left.+\exp[k_2(\lambda_{CF,2}-1)^2](\lambda_{CF,2}-1)\right]\right\}.\end{aligned} \tag{10}$$

The analytical model response was computed using a MATLAB script (version R2018b, The MathWorks, Inc., USA) and compared with the experimental results of Sommer et al. (2013), who conducted planar biaxial extension and triaxial simple shear tests on human abdominal adipose tissue. For comparison and to determine the material parameters, the results of specimen VIII under planar biaxial extension in the longitudinal direction for stretch ratios of $\lambda_1 : \lambda_2 = 1:1, 1:0.5, 0.5:1$ and under simple shear in $r\theta$ mode and rz mode were used, as these modes are expected to be most relevant for blunt impacts corresponding to shear deformation parallel to the body surface. The definition of the directions can be found in Fig. A.1 in Appendix A.

The respective material parameters were evaluated by curve fitting to the experimental data under equibiaxial tension using a nonlinear least squares method with bi-squared weights in MATLAB (version R2018b, The MathWorks, Inc., USA). It was assumed that the resulting coefficients also yield reasonable results for the other loading cases if the model assumptions are able to correctly reflect the microstructural aspects of the SAT. To analyze the robustness of the fitting, a cycle of 1 000 valid fits with random starting values between −1 and 1 for the material parameters was performed and the resulting material parameters, the coefficient of determination R^2 and the sum of squared errors SSE for each fit as well as the respective means and standard deviations over all fits were evaluated. The term valid here refers to fits that satisfied the material parameter requirements $c \geq 0$, $k_1 \geq 0$, $k_2 \geq 0$. For the fitting procedure, both the experimental data and the material parameters were expressed in kPa.

To compare the performance of the CFM with that of a state-of-the-art model, the described fitting method was also performed for a third-order Ogden model, which was successfully applied by Sun et al. (2021a) to represent the behavior of SAT in uniaxial compression as well as in simple shear. The respective SEF and the explicit expressions for the stress components for equibiaxial tension and simple shear can be found in Appendix B. Valid fits for the Ogden model had to satisfy the requirement $\alpha_1\mu_1 + \alpha_2\mu_2 + \alpha_3\mu_3 \geq 0$. For both models, the material parameters of the fit that yielded the lowest SSE were chosen as the final parameter set. To evaluate the performance of the CFM and Ogden models, the analytical results in biaxial tension and simple shear were compared with the experimental data using the EEARTH method. This method, implemented via a script in MATLAB, compares the agreement of two curves in terms of phase, magnitude, and slope, resulting in an EEARTH-score, say ES, between 0 and 1, where 0 means no agreement and 1 means perfect agreement (ISO/T.R. 16250:2013(E), 2013; ISO/T.S. 18571:2014(E), 2014). In addition, the calculation time in MATLAB over 10 000 cycles for each loading scenario was compared for both models.

3.2. Finite element setup

For the FE implementation, the CFM was evaluated in single element tests under biaxial tension and simple shear. The element edge length was set to 1 mm and a constant deformation was applied over a prescribed velocity of 1 mm/s in the respective loading directions. As element formulation, a one-point integration scheme was chosen in combination with a viscous hourglass control and an hourglass coefficient of 0.1. The material parameters evaluated according to Section 3.1 were used and κ was set to 219.2 kPa, which was calculated via the Lamé constants ($\nu = 0.499$). All simulations were computed on one CPU core (Intel®Xeon®CPU E5-2650 v4, 2.20 GHz, Intel Corporation, USA) using the explicit FE solver LS-DYNA (version R9.1, Livermore Software Technology, USA) with double precision and a time step scaling factor of 0.7. The stress-deformation results were then compared between simulation and analytical solution. In order to compare the stress-deformation results between simulation and analytical solution in the deformation regime relevant for the corresponding experiments, the EEARTH method implemented as a MATLAB script was used.

In the next step, the experiments described in the study of Sommer et al. (2013) were simulated with the CFM. The corresponding FE setups are depicted in Fig. 3. To transfer the biaxial tension setup into a FE model, the adipose tissue specimen was modeled as a square sheet with dimensions of $40 \times 40 \times 5\,\text{mm}^3$ using hexahedral elements with an edge length of 1 mm. The equibiaxial deformation was reproduced by applying a prescribed velocity of 4 mm/min in the x- and z-direction for the nodes on the respective side faces of the sheet. To introduce further stretch ratios ($1:0.5, 0.5:1$), corresponding ratios for $v_x : v_z$ were implemented. The x-distance between two nodes at the center of the specimen was tracked to analyze the corresponding stretch via the relationship $\lambda_1 = (\Delta_{biax}/\Delta_{biax,in})$, Δ_{biax} and $\Delta_{biax,in}$ depicting the actual and initial node distance of 10 mm, respectively. In addition, the section force in the x-direction on the right sheet face F_{biax} was evaluated to calculate the Cauchy stress using the equation $\sigma_1 = (F_{biax}/A_{biax,in})\lambda_1$, where $A_{biax,in}$ is the initial area of the sheet face. To reproduce the shear test setup, the adipose tissue specimen was modeled as a cuboid

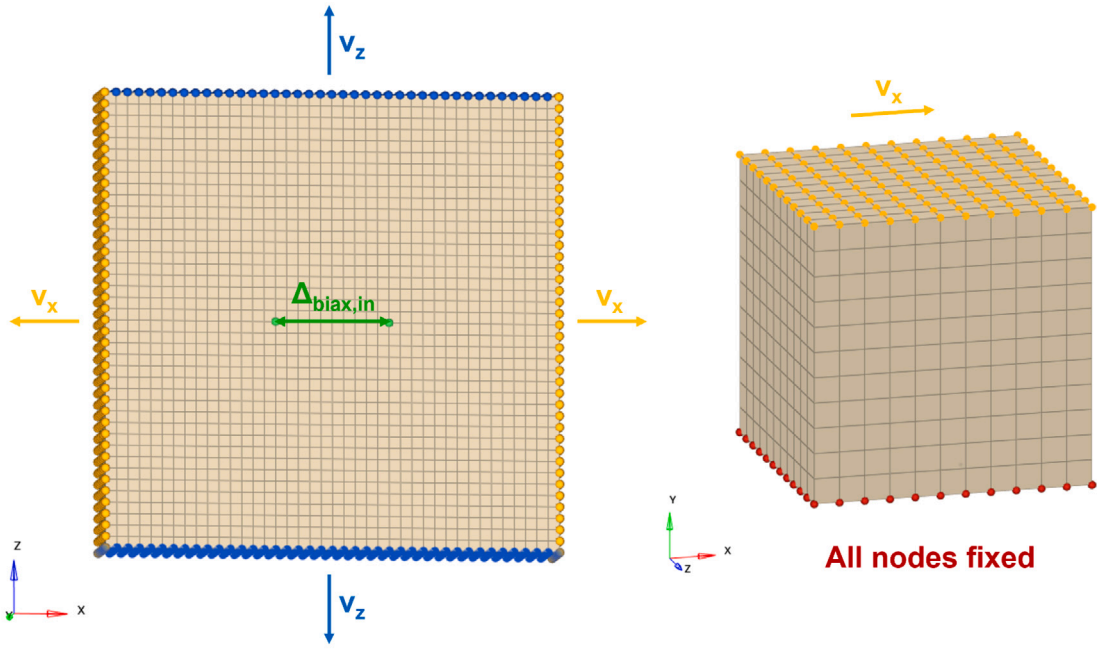

Fig. 3. FE models of the biaxial tensile test setup (left) and the simple shear test setup (right) according to the experiments of Sommer et al. (2013). The boundary conditions were applied according to the experimental test conditions and applied to node sets represented as spheres in the color of the respective boundary condition.

with an edge length of 8 mm using hexahedral elements with a size of 0.7 mm. A prescribed velocity of 1 mm/min in the x-direction was set for all nodes on the top surface of the specimen. All degrees of freedom were fixed for the nodes on the bottom surface of the specimen, and all degrees of freedom, except translation in the x-direction, were constrained for the nodes on the top surface of the specimen. As output, the reaction force F_{shear} of the bottom surface of the specimen and the displacement Δ_{shear} of the corner node in the x-direction were evaluated. The stress–strain curve was calculated using the relationships $\gamma = \Delta_{\text{shear}}/L_{\text{shear,in}}$ and $\sigma_{12} = F_{\text{shear}}/A_{\text{shear,in}}$, where $L_{\text{shear,in}}$ and $A_{\text{shear,in}}$ are the initial specimen length and area, respectively. For both FE setups, element formulation, material parameters and simulation settings were the same as for the single element tests, except that four CPU cores were used for each simulation instead of one. To evaluate the model behavior, the agreement between the simulation results and the respective experimental data from Sommer et al. (2013) were examined using the EEARTH method (ISO/T.R. 16250:2013(E), 2013; ISO/T.S. 18571:2014(E), 2014).

4. Results

4.1. Fitting results and material parameters

Tables 1 and 2 show the results for the best fit and the corresponding means and standard deviations over all 1 000 fits for the CFM, i.e. Eqs. (1)–(3), and the Ogden model, i.e. Eq. (B.1). The CFM exhibits a fairly robust fitting performance — the material parameters resulting from the best fit are almost equal to the mean values of the corresponding parameters over all fits and the respective standard deviation is quite small. In contrast, for the Ogden model, a large difference can be seen between the material parameters of the best fit and the corresponding mean values, which also have a considerable standard deviation. The coefficient of determination is quite high for both models with respect to the best fit, but also the average over all fits.

Since the fitting was only performed on the experimental data at equibiaxial tension, in Fig. 4 the analytical results of the CFM and Ogden models are compared with the experimental results of Sommer et al. (2013) for all investigated load cases. In biaxial tension, both models can capture the experimental results quite well, which is also reflected in quite high EEARTH values. However, in simple shear, the analytical solution of the CFM is too stiff, while that of the Ogden model is too soft compared to the experimental data. However, with an EEARTH score of 0.81, the analytical response of the CFM can at least provide a reasonable agreement with the experimental result in rz-mode. In addition, the calculations with the CFM were quite efficient. Compared to the Ogden model, the calculation time was about 30 times faster in biaxial tension and about 10 times faster in simple shear, as can be seen in Fig. 4.

4.2. Finite element setups

Fig. 5 depicts a comparison between the numerical simulation results of the single element tests and the analytical solution of the CFM. It can be seen that the implementation of the CFM as a user-defined material was successful. The simulations were stable up to the deformations relevant for the experimental loading scenarios and a reasonable agreement between analytical and numerical solution could be achieved, which is indicated by EEARTH scores of at least 0.99 for all load cases.

Acceptable results for the CFM were also obtained in the numerical simulation of the component test setups. A comparison of the simulation results with the experimental data of Sommer et al. (2013) is shown in Fig. 6. For biaxial tension, the simulation results agree well with the experimental data. In fact, the picture is quite similar to that for the analytical model solution and also the EEARTH scores are the same for the simulation and the analytical outcome (compare also Fig. 4). However, for simple shear, the material response is softer compared to that of the analytical solution, but also to that of the simulation result for the single element test. This leads to significantly better EEARTH scores of at least 0.90 for the comparison of the results of the shear test setup simulations with the experimental data for both modes of simple shear.

Table 1
Material parameters (c, k_1, k_2), coefficient of determination (R^2) and sum of squared errors (SSE) for the best fit as well as the respective mean value and standard deviation (SD) over all fits for the CFM; material parameters refer to Eqs. (1)–(3).

CFM	c [kPa]	k_1 [kPa]	k_2 [−]	R^2 [−]	SSE [−]
Best fit	0.00947	0.429	11.6	0.994	0.0219
Mean	0.00951	0.429	11.6	0.994	0.0219
± SD	5.43×10^{-6}	1.08×10^{-5}	1.97×10^{-4}	3.15×10^{-9}	1.23×10^{-8}

Table 2
Material parameters (μ_1, α_1, μ_2, α_2, μ_3, α_3), coefficient of determination (R^2) and sum of squared errors (SSE) for the best fit as well as the respective mean value and standard deviation (SD) over all fits for the third-order Ogden model; material parameters refer to Eq. (B.1) .

Ogden	μ_1 [kPa]	α_1 [−]	μ_2 [kPa]	α_2 [−]	μ_3 [kPa]	α_3 [−]	R^2 [−]	SSE [−]
Best fit	−2.92	−0.843	−0.701	3.34	-5.87×10^{-4}	−23.1	0.997	0.0134
Mean	0.0544	−5.03	0.134	−5.16	−0.00232	−4.42	0.964	0.141
± SD	1.36	4.69	1.34	4.67	1.42	4.51	0.0757	0.296

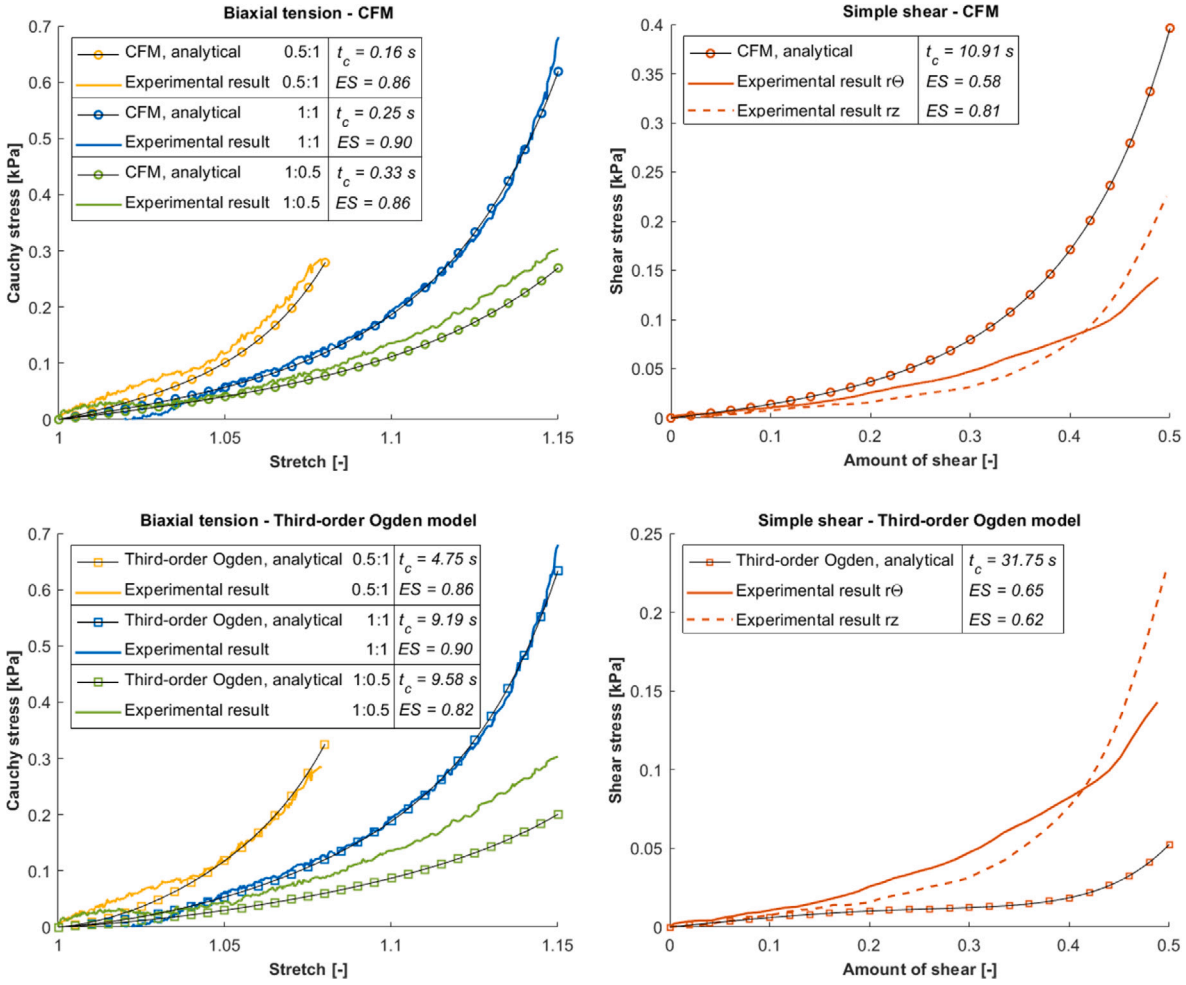

Fig. 4. Analytical results for the CFM and Ogden models under biaxial tension and simple shear compared to the experimental data from Sommer et al. (2013) with corresponding computation time t_c over 10 000 cycles and EEARTH score ES for the analytical solutions. The fitting of the material parameters was based solely on the experimental data under equibiaxial tension. The resulting material parameters were used to calculate the analytical solutions for the other load cases.

5. Discussion

In this study, a material model for SAT under blunt impact was developed and analyzed in both an analytical and numerical context. Model development was based on the microstructural components of the SAT with focus on the RBM. The performance of the developed model was investigated using experimental data under biaxial tension and simple shear (Sommer et al., 2013), although blunt impact mainly involves compression and shear loads. However, uniaxial compression and biaxial tension are related because the specimen is stretched in two directions and gets compressed or, in the case of biaxial tension, contracted in the third direction. In addition, the material response under biaxial tension is believed to be less affected by effects such as friction and thus provides a more appropriate basis for model evaluation. Furthermore, biaxial testing allows for a larger data base by applying different stretch ratios in the two test directions.

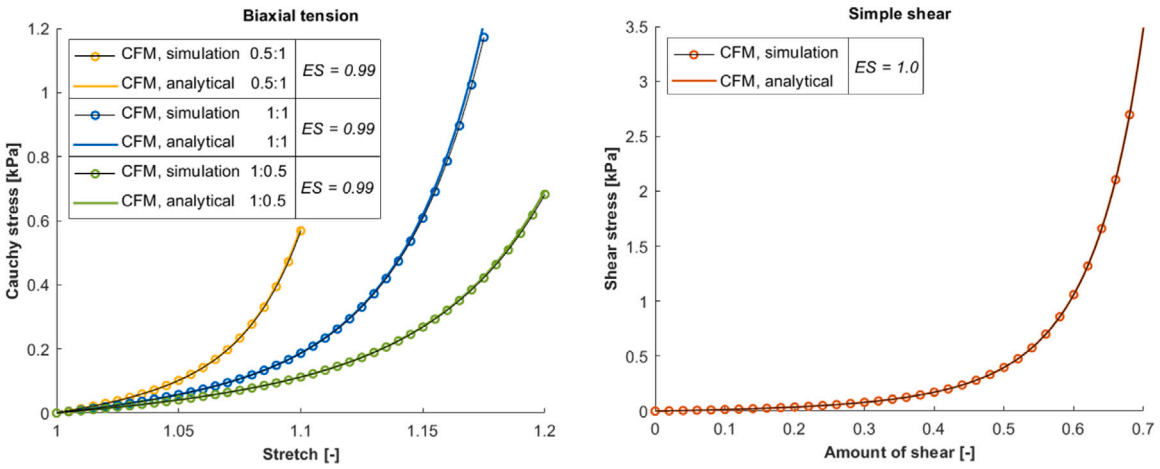

Fig. 5. Numerical simulation results of the single element tests for the CFM under biaxial tension and simple shear compared to the analytical solution and the resulting EEARTH score ES.

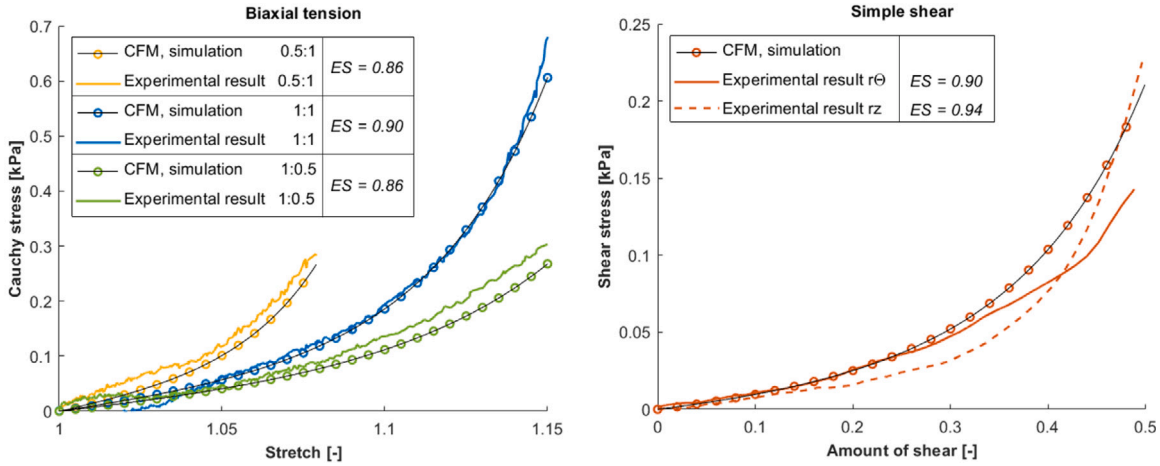

Fig. 6. Numerical simulation results of the component test setups under biaxial tension and simple shear for the CFM in comparison with the experimental data from Sommer et al. (2013) and the corresponding EEARTH score ES.

The analytical fit of the CFM to the experimental data at equibiaxial tension proved to be quite robust. The similarity between the resulting values for the best fit and the respective mean values across all fits indicates that a clear minimum was found. For the third-order Ogden model, however, the results for the material parameters of the best fit show a large difference from the respective mean values of all fits. In combination with the evaluated high standard deviation, this implies that the results depend strongly on the chosen starting values for the respective fit. One reason for this could be that the Ogden model is purely phenomenological, while the CFM takes the microstructure of the tissue into account. To check whether the microstructural model assumptions of the CFM are reasonable, the fit was only performed to the data at equibiaxial tension, assuming that the resulting material parameters would also provide reasonable results for the other load cases with a good modeling approach. For biaxial tension, the analytical solution of both the CFM and the Ogden model showed a good agreement with the experimental data. However, for simple shear, a better agreement could be observed for the CFM, at least in comparison with the shear data in rz-mode, suggesting that the model assumptions of the CFM are reasonable. This is further supported by the results of the numerical simulations of the experiments in Sommer et al. (2013) using the CFM. While the results for biaxial tension exhibit a similarly satisfactory outcome as for the analytical solution compared to the experimental data, the results for simple shear show a far better agreement with the experimental data than for the analytical solution, which is also reflected in the EEARTH scores of at least 0.90. It is assumed that this difference is not due to an incorrect FE implementation of the CFM, since the EEARTH score for the comparison between the simulation result for the single element tests and for the analytical solution of the CFM under simple shear was 1.0, but rather due to the experimental conditions. Due to the very soft nature of the adipose tissue and the cubic specimen geometry, the deformation in the experiments may not have perfectly represented simple shear, but was slightly superimposed by other modes of deformation. The CFM also appears promising in terms of computation time, since the calculation of the analytical model solution under biaxial tension and under simple shear is significantly shorter than for the third-order Ogden model.

The comparison with this model was made because, to the authors' knowledge, Sun et al. (2021a) were the first to successfully solve the problem of simultaneously modeling SAT under uniaxial compression and simple shear using the third-order Ogden model. In a previous study, the authors of Sun et al. (2021b) performed uniaxial compression as well as simple shear tests on human adipose tissue and found that a first-order Ogden model was not sufficient to represent the material response for the different loading scenarios simultaneously. In fact, Sommer et al. (2013) were the first to recognize this problem. They not only studied SAT experimentally but also modeled its behavior under biaxial tension and simple shear using a model that was established for fiber-reinforced soft tissue. Furthermore, the authors observed larger deviations between model solution and experimental

data for a combined fit to both loading scenarios compared to fits to each loading scenario separately. Sun et al. (2021a) conducted their analyses in the context of vehicle occupant loading and aimed to model the behavior of SAT during collisions, in particular to investigate the interaction of the restraint system with the abdomen. In this context, a phenomenological model such as the third-order Ogden model seems to be a suitable approach, since for such scenarios the energy absorption of the SAT considered as a bulk material is supposed to be relevant. However, for a deeper investigation of blunt impacts and the associated injury mechanisms, more localized effects need to be considered. In this context, microstructurally motivated models such as the CFM can be beneficial, especially since the mechanics of blunt force trauma have not yet been fully understood using experimental methods (Dempsey and Blau, 2020). Numerical simulations may be better suited to answer this question because, unlike experimental methods, stresses and strains can be assessed at the tissue level (Cronin, 2011; Dempsey and Blau, 2020).

This study has several limitations. First, the model performance was analyzed using the experimental data of a single specimen. The main intention of this analysis was to investigate whether the developed CFM and the underlying microstructural assumptions can reproduce the mechanical behavior of SAT under different loading cases. However, this is challenging because SAT exhibits a large inter- but also intra-individual variability (Sommer et al., 2013; Sun et al., 2021a). Sommer et al. (2013) performed an analytical fit to the experimental data of specimens from different donors and obtained different material parameters for each fit, suggesting inter-individual differences in the material response. Sun et al. (2021a) were also able to detect large deviations in their experimental data and provide variability between the different donors as a possible explanation. More specifically, they state that differences in individual microstructure, especially in the volume fraction and properties of the RBM, could be responsible for these deviations. Since the CFM mainly focuses on the behavior of the RBM within the SAT, data from only one specific donor were used to verify the assumptions that form the theoretical basis for the developed model. This made it possible to evaluate the performance of the model and ensure that effects due to biological variability were excluded as much as possible and did not confound the outcome of the analysis.

Another limitation is that the first version of the model does not consider the behavior of the septa fibers, which are supposed to be responsible for the anisotropic behavior of the SAT (Sommer et al., 2013). However, the anisotropic nature of the SAT is not fully understood to date. In addition to their experiments, Sommer et al. (2013) also performed a histological analysis of the tested specimens, but were unable to determine a preferred orientation of the septa fibers within the tissue. Sun et al. (2021a) used scanning electron microscopy to investigate the microstructure of the SAT and were also unable to determine a preferred alignment of the septa fibers, although the specimens showed a clear direction during the experiments. For a meaningful inclusion of the septa fibers and thus the anisotropic material response, at least further information on the fiber orientation is required, which could be achieved by combining imaging techniques such as histological analysis or multiphoton microscopy and experimental testing. If such data are available, the SEF of the CFM can be coupled with an additional term for the septa fibers, similar to the one presented in Sommer et al. (2013).

In addition, the FE implementation of the CFM was performed as a user-defined material using the deviatoric and volumetric split, which is known to introduce errors regarding the accuracy of the numerical solution (Gültekin et al., 2019). Particular concerns are that the decomposition is not physically realistic, especially for anisotropic materials, and that it is unable to represent linear anisotropic elasticity in the low-strain regime (Ní Annaidh et al., 2013; Vergori et al., 2013; Nolan et al., 2014). However, the intended application of the finalized material model is the investigation of blunt force impacts with high (non-physiological) deformations and high impact velocities, but not deformations in the low-strain regime. Moreover, the focus of the present paper is on the formulation and characterization of the material model itself, not on its FE implementation. The underlying model formulation is not based on this split, and verification by single-element tests with biaxial tension and simple shear confirms that the simulation results are in close agreement with the analytical solutions in the relevant deformation range. This is not only shown by the visual comparison of the resulting curves, but is also confirmed by an objective rating method, i.e., by EEARTH scores of at least 0.99 for the comparison between the analytical and the simulation results.

Sommer et al. (2013) observed a failure stretch of about 1.21 for adipose tissue tested under equibiaxial tension, compared to the stretch range of 1.15 analyzed in the present study, and therefore a suitable damage and failure model would need to be implemented also for higher deformations. Another drawback of deviatoric and volumetric split is that the material parameters deviate from those originally calibrated under the assumption of perfect incompressibility. However, the main goal of this study was to demonstrate the intrinsic robustness and predictive capability of the constitutive model itself. The material parameters were therefore not adjusted for the FE implementation to allow an unbiased evaluation of the model performance. The agreement of the analytical solution with the simulation results presented in Section 4.2 shows that the model is robust to small variations in the parameter values. However, the FE implementation needs to be re-evaluated in a future work — especially when the model is extended to include septa fibers for anisotropic mechanical behavior.

Finally, the model does not yet account for strain rate dependence, which is essential for investigating blunt force trauma. This is also the reason why a direct comparison of the CFM with the experimental data in Sun et al. (2021a) was not possible, since the respective authors performed their experiments at strain rates between 3 and $50\,s^{-1}$. However, strain rate dependence can be implemented independently of the applied hyperelastic model via, e.g., a normalized relaxation function represented by a Prony series (Payne et al., 2015; Calvo-Gallego et al., 2018; Sun et al., 2021a). And since the focus of the present study was on evaluating the developed CFM and the underlying theory, the implementation of rate effects is considered as a next step, using, e.g., the data in Sun et al. (2021a) as an experimental basis.

6. Conclusion and outlook

In this study, a microstructurally motivated material model for SAT was developed within the framework of nonlinear continuum mechanics and implemented as a user-defined material model in the FE solver LS-DYNA. The focus of the first model version was on the behavior of the RBM, the collagenous structure surrounding the adipocytes and represented by three circular fiber families. The model is able to reproduce the experimental behavior of SAT in different modes of biaxial tension and in simple shear simultaneously quite well. A next step is to extend the model to represent the strain rate dependent behavior, as this is essential for studying blunt force trauma. In addition, it should be updated to account for the behavior of the septa fibers as more data on their orientation within the SAT become available. With the introduction of septa fibers and the resulting anisotropy, the FE implementation of the model needs to be revised to address potential errors introduced by the use of volumetric and deviatoric decomposition for anisotropic models. Taking the microstructure of the SAT into account, the developed CFM could help to further investigate the injury mechanisms of blunt impact and develop more objective methods to assess the impact forces required to generate a specific injury.

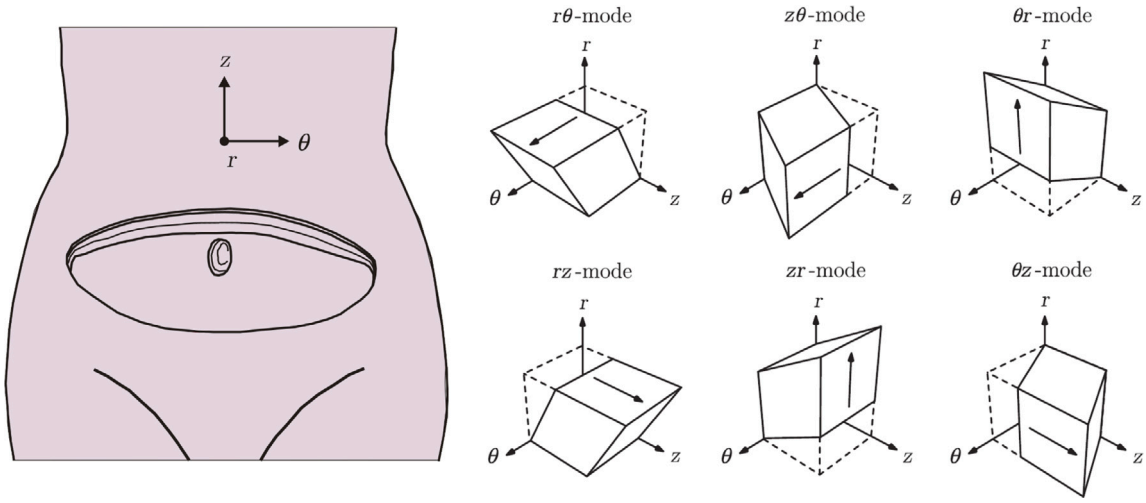

Fig. A.1. Orientation of the specimen in relation to the human body for the experimental setups. The transverse, longitudinal and sagittal body directions are represented by the θ-axis, the z-axis and the r-axis, respectively (figure after Sommer et al. (2013)).

CRediT authorship contribution statement

Felicitas Lanzl: Writing – original draft, Visualization, Validation, Software, Methodology, Investigation, Formal analysis, Data curation, Conceptualization. **Steffen Peldschus:** Writing – review & editing, Supervision, Resources, Conceptualization. **Gerhard A. Holzapfel:** Writing – review & editing, Visualization, Supervision, Conceptualization. **Fabian Duddeck:** Writing – review & editing, Supervision, Formal analysis, Conceptualization. **Gerhard Sommer:** Writing – review & editing, Visualization, Validation, Supervision, Methodology, Data curation, Conceptualization.

Declaration of competing interest

The authors declare that they have no known competing financial interests or personal relationships that could have appeared to influence the work reported in this paper.

Appendix A. Specimen orientation

Fig. A.1 shows the orientation of the specimens used in the experiments of Sommer et al. (2013) with respect to the human body. Biaxial specimens were stretched along the θ-axis and the z-axis, which correspond to the transverse and longitudinal axes of the body, respectively. Shear tests were performed with respect to six different specimen orientations.

Appendix B. Third-order Ogden model

The strain–energy function of the first-order Ogden model is (Ogden, 1972)

$$\Psi = \sum_{p=1}^{3} \frac{\mu_p}{\alpha_p}(\lambda_1^{\alpha_p} + \lambda_2^{\alpha_p} + \lambda_3^{\alpha_p} - 3), \tag{B.1}$$

where μ_1, μ_2 and μ_3 are material parameters with the dimension stress and α_1, α_2 and α_3 are dimensionless material parameters (Ogden, 1972). The analytical solution of the third-order Ogden model for biaxial tension with equibiaxial stretch along the first and second principal axes $\lambda_1 = \lambda_2 = \lambda$ is (Holzapfel, 2000)

$$\sigma_i = \sum_{p=1}^{3} \mu_p\left(\lambda^{\alpha_p} - \lambda^{-2\alpha_p}\right), \qquad i = 1, 2. \tag{B.2}$$

The analytical solution of the third-order Ogden model in simple shear for a deformation by the amount of shear γ is given by

$$\sigma_{12} = \frac{1}{2\sqrt{1+\frac{\gamma^2}{4}}}\left\{\sum_{p=1}^{3} \mu_p\left[\left(\frac{\gamma}{2} + \sqrt{1+\frac{\gamma^2}{4}}\right)^{\alpha_p} - \left(\frac{\gamma}{2} + \sqrt{1+\frac{\gamma^2}{4}}\right)^{-\alpha_p}\right]\right\}. \tag{B.3}$$

Data availability

Data will be made available on request.

References

Alkhouli, N., Mansfield, J., Green, E., Bell, J., Knight, B., Liversedge, N., Tham, J.C., Welbourn, R., Shore, A.C., Kos, K., Winlove, C.P., 2013. The mechanical properties of human adipose tissues and their relationships to the structure and composition of the extracellular matrix. Am. J. Physiol, Endocrinol. Metab. 305 (12), E1427–E1435.

Calvo-Gallego, J.L., Domínguez, J., Gómez Cía, T., Gómez Ciriza, G., Martínez-Reina, J., 2018. Comparison of different constitutive models to characterize the viscoelastic properties of human abdominal adipose tissue. a pilot study. J. Mech. Behav. Biomed. Mater. 80, 293–302.

Chun, T.-H., 2012. Peri-adipocyte ECM remodeling in obesity and adipose tissue fibrosis. Adipocyte 1 (2), 89–95.

Comley, K., Fleck, N.A., 2010a. A micromechanical model for the Young's modulus of adipose tissue. Int. J. Solids Struct. 47 (21), 2982–2990.

Comley, K., Fleck, N.A., 2010b. The toughness of adipose tissue: measurements and physical basis. J. Biomech. 43 (9), 1823–1826.

Comley, K., Fleck, N., 2012. The compressive response of porcine adipose tissue from low to high strain rate. Int. J. Impact Eng. 46, 1–10.

Cronin, D.S., 2011. Explicit finite element method applied to impact biomechanics problems. Proceedings of the International Research Council on the Biomechanics of Injury Conference, Proceedings of the International Research Council on the Biomechanics of Injury Conference, vol. 39.240–254,

Daly, C.H., 1982. Biomechanical properties of dermis. J. Invest. Dermatol. 79 (1, Supplement), 17–20.

Dempsey, N., Blau, S., 2020. Evaluating the evidentiary value of the analysis of skeletal trauma in forensic research: A review of research and practice. Forensic Sci. Int. 307, 110140.

Gültekin, O., Dal, H., Holzapfel, G.A., 2019. On the quasi-incompressible finite element analysis of anisotropic hyperelastic materials. Comput. Mech. 63, 443–453.

Gurdjian, E.S., 1972. Recent advances in the study of the mechanism of impact injury of the head – a summary. Neurosurgery 19, 1–42.

Holzapfel, G.A., 2000. Nonlinear Solid Mechanics. A Continuum Approach for Engineering. John Wiley and Sons.

Holzapfel, G.A., 2001. Section 10.11 – biomechanics of soft tissue. In: Lemaitre, J. (Ed.), Handbook of Materials Behavior Models. Academic Press, Burlington, pp. 1057–1071.

Holzapfel, G.A., Gasser, T.C., Ogden, R.W., 2000. A new constitutive framework for arterial wall mechanics and a comparative study of material models. J. Elasticity 61, 1–48.

Horgan, C., Murphy, J., 2010. Simple shearing of incompressible and slightly compressible isotropic nonlinearly elastic materials. J. Elasticity 98, 205–221.

ISO/T.R. 16250:2013(E), 2013. Road vehicles – Objective rating metrics for dynamic systems. International Organization for Standardization, Geneva, CH.

ISO/T.S. 18571:2014(E), 2014. Road vehicles – Objective rating metric for non-ambiguous signals. International Organization for Standardization, Geneva, CH.

Kieser, J., 2012. Biomechanics of skin and soft tissue trauma. In: Forensic Biomechanics. John Wiley & Sons, pp. 71–97.

Lanzl, F., Duddeck, F., Willuweit, S., Peldschus, S., 2022. Experimental characterisation of porcine subcutaneous adipose tissue under blunt impact up to irreversible deformation. Int. J. Legal Med. 136 (3), 897–910.

Naseri, H., Johansson, H., Brolin, K., 2018. A nonlinear viscoelastic model for adipose tissue representing tissue response at a wide range of strain rates and high strain levels. J. Biomech. Eng. 140 (4), 041009–1–041009–8.

Ní Annaidh, A., Destrade, M., Gilchrist, M., Murphy, J., 2013. Deficiencies in numerical models of anisotropic nonlinearly elastic materials. Biomech. Model. Mechanobio. 12, 781–791.

Nikolić, V., Hančević, J., Hudec, M., Banović, B., 1975. Absorption of impact energy in palmar soft tissues. Anat. Embryol. 148, 215–221.

Nolan, D., Gower, A., Destrade, M., Ogden, R., McGarry, J., 2014. A robust anisotropic hyperelastic formulation for the modelling of soft tissue. J. Mech. Behav. Biomed. Mater. 39, 48–60.

Ogden, R.W., 1972. Large deformation isotropic elasticity: on the correlation of theory and experiment for compressible rubberlike solids. Proc. R. Soc. Lond. A328, 567–583.

O'Hagan, J., Samani, A., 2009. Measurement of the hyperelastic properties of 44 pathological ex vivo breast tissue samples. Phys. Med. Biol. 54, 2557–2569.

Payne, T., Mitchell, S., Bibb, R., Waters, M., 2015. Development of novel synthetic muscle tissues for sports impact surrogates. J. Mech. Behav. Biomed. Mater. 41, 357–374.

Quatrehomme, G., Alunni, V., 2019. The link between traumatic injury in soft and hard tissue. Forensic Sci. Int. 301, 118–128.

Rivlin, R.S., Taylor, G.I., 1948. Large elastic deformations of isotropic materials. I. Fundamental concepts. Philos. Trans. A Math. Phys. Eng. Sci. 240 (822), 459–490.

Sharkey, E.J., Cassidy, M., Brady, J., Gilchrist, M.D., NicDaeid, N., 2012. Investigation of the force associated with the formation of lacerations and skull fractures. Int. J. Legal Med. 126 (6), 835–844.

Sheldon, H., 2011. Morphology of adipose tissue: a microscopic anatomy of fat. In: Comprehensive Physiology. American Cancer Society, pp. 125–139.

Sommer, G., Eder, M., Kovacs, L., Pathak, H., Bonitz, L., Müller, C., Regitnig, P., Holzapfel, G.A., 2013. Multiaxial mechanical properties and constitutive modeling of human adipose tissue: a basis for preoperative simulations in plastic and reconstructive surgery. Acta. Biomater. 9, 9036–9048.

Sree, V.D., Toaquiza-Tubon, J.D., Payne, J., Solorio, L., Buganza Tepole, A., 2023. Damage and fracture mechanics of porcine subcutaneous tissue under tensile loading. Ann. Biomed. Eng. 51 (9), 2056–2069.

Sun, Y., Chen, L., Yick, K.-L., Yu, W., Lau, N., Jiao, W., 2019. Optimization method for the determination of mooney-rivlin material coefficients of the human breasts in-vivo using static and dynamic finite element models. J. Mech. Behav. Biomed. Mater. 90, 615–625.

Sun, Z., Gepner, B.D., Lee, S.-H., Rigby, J., Cottler, P.S., Hallman, J.J., Kerrigan, J.R., 2021a. Multidirectional mechanical properties and constitutive modeling of human adipose tissue under dynamic loading. Acta Biomater. 129, 188–198.

Sun, Z., Lee, S.-H., Gepner, B.D., Rigby, J., Hallman, J.J., Kerrigan, J.R., 2021b. Comparison of porcine and human adipose tissue loading responses under dynamic compression and shear: A pilot study. J. Mech. Behav. Biomed. Mater. 113, 104112.

Treloar, L.R.G., 1943. The elasticity of a network of long-chain molecules – II. Trans. Faraday Soc. 39, 241–246.

Treloar, L.R.G., 1944. Stress-strain data for vulcanised rubber under various types of deformation. Trans. Faraday Soc. 40, 59–70.

Trotta, A., Ní Annaidh, A., 2019. Mechanical characterisation of human and porcine scalp tissue at dynamic strain rates. J. Mech. Behav. Biomed. Mater. 100, 103381.

Trotta, A., Zouzias, D., De Bruyne, G., Ní Annaidh, A., 2018. The importance of the scalp in head impact kinematics. Ann. Biomed. Eng. 46, 831–840.

Vergori, L., Destrade, M., McGarry, P., Ogden, R.W., 2013. On anisotropic elasticity and questions concerning its finite element implementation. Comput. Mech. 52 (5), 1185–1197.